Mesoscale weather systems and associated potential wind power variations in a mid-latitude sea strait (Kattegat)

Jérôme Neirynck[1], Jonas Van de Walle[1], Ruben Borgers[1], Sebastiaan Jamaer[1], Johan Meyers[2], Ad Stoffelen[3], and Nicole P.M. van Lipzig[1]

[1]Earth and Environmental Sciences, KU Leuven, Belgium
[2]Mechanical Engineering, KU Leuven, Belgium
[3]R&D Satellite Observations, Royal Netherlands Meteorological Institute, De Bilt, The Netherlands

Correspondence: Jérôme Neirynck (jerome.neirynck@kuleuven.be)

Abstract. Mesoscale weather systems cause spatiotemporal variability in offshore wind power and insight in their fluctuations can support grid operations. In this study, a 10-year model integration with the kilometre-scale atmospheric model COSMO-CLM served a wind and potential power fluctuation analysis in the Kattegat, a mid-latitude sea strait of 130 km width with an irregular coastline. The model agrees well with scatterometer data away from coasts and small islands, with a spatiotemporal root mean square difference of 1.35 m/s. A comparison of 10 minute wind speed at about 100 metre with lidar data for a 2 year period reveals a very good performance with a slight model overestimation of 0.08 m/s and a high value for the Perkins Skill Score (0.97). From periodograms made using the Welch method it was found that the wind speed variability on a sub-hourly timescale is higher in winter compared to summer. In contrast, the wind power varies more in summer when winds often drop below the rated power threshold. During winter, variability is largest in the northeastern part of the Kattegat due to a spatial spin up of convective systems over the sea during the predominant southwesterly winds. Summer convective systems are found to develop over land, driving spatial variability in offshore winds during this season. On average over the 10 summers the mesoscale wind speeds are up to 20% larger than the synoptic background at 17 UTC with a clear diurnal cycle. The winter averaged mesoscale wind component is up to 10% larger with negligible daily variation. Products with a lower resolution like ERA5 substantially underestimate this ratio between the mesoscale and synoptic wind speed. Moreover, taking into account mesoscale spatial variability is important for correctly representing temporal variability of power production. The root mean square difference between two power output time series, one ignoring and one accounting for mesoscale spatial variability, is 14% of the total power generation.

Keywords. Regional climate modelling, mesoscale systems, wind speed variability, wind power fluctuations

1 Introduction

According to the sixth iteration of the Intergovernmental Panel on Climate Change (IPCC) assessment report wind energy is one of the capital ways of reducing greenhouse gas emissions (Shukla et al., 2022). Therefore, offshore wind energy will be playing an increasingly important role in our electricity grid. Compared to onshore, offshore locations are advantageous
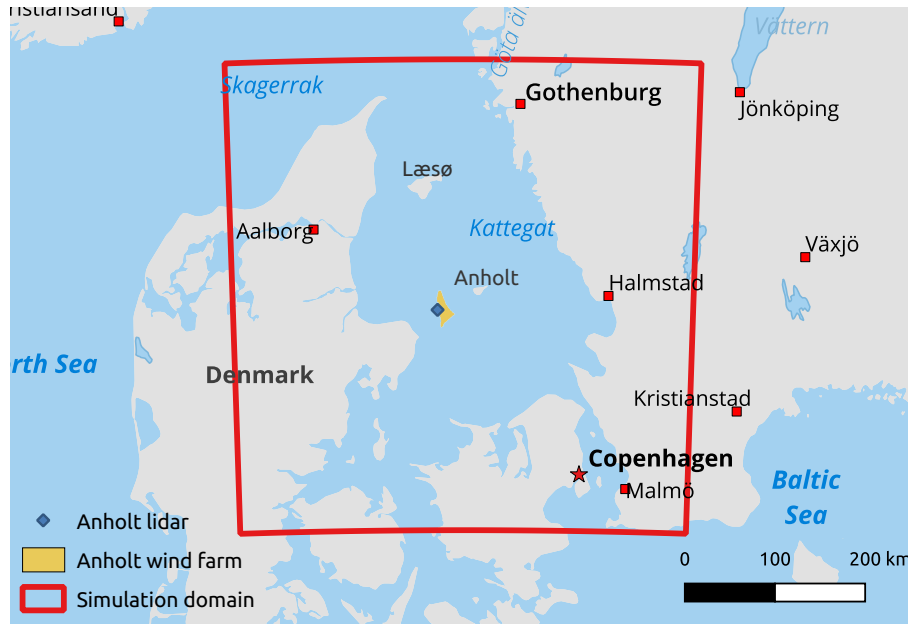
Figure 1. Map of the simulation domain. On every side of the domain 20 points are used for relaxation and spin up zones. These relaxation and spin up points are not used in the analysis. Made with Natural Earth.

because the offshore environment generally features greater wind speeds (Kaldellis and Kapsali, 2013). Additionally they also have a higher acceptance in society since offshore wind turbines are mostly placed out of sight (Betakova et al., 2015).

25

Over the years, individual wind turbines have grown significantly in size and offshore wind project areas are now much bigger than ten years ago, thereby strongly condensing the power generating capacity (Díaz and Soares, 2020). Hence, such condensed wind farms are having a direct impact on the power grid. In addition, in the absence of large energy storage facilities, electricity production always needs to match demand (Hossain and Pota, 2014). A condensed wind farm with low production

30   during the peak demand hours is detrimental. In brief, with changing wind farm layout and challenging energy demand, wind variations at increasingly fine spatial and temporal scales have to be investigated. As an example, a thunderstorm system passing a condense wind farm during peak energy demand hours is expected to generate large power fluctuations affecting the power grid. This effect is amplified by the fact that the power output of a wind turbine is related to the cube of the wind speed. Knowing when to expect these power fluctuations is of great interest for grid operators.

35

The passing of synoptic weather systems is a driver for wind power fluctuations on a timescale of multiple days (Kempton et al., 2010; Grams et al., 2017). For example depressions and associated fronts (Ahrens, 1994) are related to the four day peak in the spectrum defined by Van der Hoven (1957). Synoptic systems can be sufficiently resolved in relatively coarse resolution ($\mathcal{O}(10 \text{ km})$) hydrostatic weather simulations. On the other hand, turbulence manifests as small-scale chaotic motion in fluid

40   dynamics (Batchelor, 2000). It is also well known that turbulence generated by wind turbines affects turbines downstream (Calaf et al., 2010; Meyers and Meneveau, 2012; Lanzilao and Meyers, 2022). The effects of turbulence can be taken into account in Large Eddy Simulations (LES) or in Reynolds Averaged Navier-Stokes (RANS) simulations (Chung et al., 2002). Their high computational cost does however pose a constraint on domain size and the duration of these simulations.

45   Less is known about mesoscale weather systems, for example in organised convection. They have length scales of up to hundred kilometres and time scales from ten minutes up to a few hours, comprising thunderstorms, but also sea breeze systems, low-level jets and gravity waves (Orlanski, 1975; Nunalee and Basu, 2014). These phenomena can be resolved in kilometre-scale non-hydrostatic models such as COSMO-CLM (Helsen et al., 2020; Thiery et al., 2015; Brisson et al., 2016; Van de Walle et al., 2020) or WRF (Peña et al., 2018; Larsén and Fischereit, 2021; Porchetta et al., 2021), either with or without

50   parameterisations for deep or shallow convection according to the models' resolution (Skamarock, 2004). Research in wind speed variability associated with mesoscale weather systems is rather limited. Sea breeze systems are the exception to this, but the majority of research is based on the onshore extent of the systems. The offshore part of sea breezes can however have an influence on the power output of a wind farm as it, in general, opposes the synoptic wind flow (Steele et al., 2015). Convective systems are also known to affect wind speed variability and a correlation between rainfall and wind speed variability is ap-

55   parent (Weusthoff and Hauf, 2008). In a coastal environment, variability is found to be dependant on the flow direction: when in autumn and winter the wind is coming from over sea rather than over land a larger variability is found over the North Sea (Vincent et al., 2011). The relatively warm sea water combined with cold air aloft creates unstable conditions, which result in mesoscale systems creating wind speed variations. But also in stable conditions systems can induce wind speed variability, for instance due to nocturnal jets or gravity waves.

60

Research on mesoscale variability is often either performed with coarser scale products (Olauson, 2018; Molina et al., 2021; Bolgiani et al., 2022) or for specific case studies (Jankov et al., 2005; Carvalho et al., 2014; Larsén and Fischereit, 2021; Müller et al., 2023). Here we use the convection permitting mesoscale climate model COSMO-CLM with a horizontal resolution of 1.5 km integrated for a period of 10 years. We focus on wind speed variability due to mesoscale weather systems, specifically

65   those occurring over sea. Furthermore, we associate the mesoscale wind speed variability with fluctuations in wind power. In order to minimise cable and maintenance costs offshore wind turbines are often built in farms near the coastline (Milborrow, 2020), implying that they are subject to coastal weather effects. This is why the Kattegat area (fig. 1) is our region of interest as it features a very irregularly shaped coastline, making it particularly interesting for studying mesoscale weather systems and their impact on wind farm power production. Moreover, it is largely surrounded by land, giving ample opportunity to study

70   how mesoscale weather systems developing over land influence offshore winds. In fact, an offshore wind farm is present in the Kattegat: the Anholt wind farm, exploited by Ørsted. The aim of this paper is to investigate what factors influence mesoscale wind speed variability, on what timescales this variability occurs, and how it affects wind power output in offshore wind farms.

The remainder of this paper is structured as follows: section 2 contains the specifications of the simulation domain and the
75 model set up (2.1) and validation (2.2), as well as the explanations of the methods used for studying the wind speed variability
(2.3 and 2.4). Next, the results are reported in section 3, where a comparison of the model output with scatterometer data
(3.1) is followed by the results for both a temporal and a spatial analysis (3.2 and 3.3). The main findings of this paper are
summarised in the concluding section.

2 Methods

2.1 Model setup

The model we use is the COnsortium for Small-scale MOdelling-CLimate Mode (COSMO-CLM) non-hydrostatic limited-area
atmospheric model (Rockel et al., 2008). COSMO-CLM is a community model which is continuously maintained and devel-
oped by its users, under the coordination of the German Weather Service (DWD). The dynamical core of this model solves the
primitive thermo-hydrodynamical equations describing a compressible flow in a moist atmosphere (Doms and Baldauf, 2018).
85 The COSMO-model uses an Arakawa C-grid and a staggered Lorenz vertical grid with terrain following Gal-Chen coordinates.
The horizontal grid is mapped out in rotated coordinates with a spacing of $0.0135°$. This corresponds to a horizontal distance
of approximately 1.5 km which allows for explicit representation of deep convection in the model. For shallow convection the
dynamical core of the model is expanded with a shallow convection parametrisation of Tiedtke (1989). Further parametrisa-
tions are present in the model that take subgrid-scale processes regarding turbulence (Raschendorfer, 2001; Schulz, 2008*a*, *b*),
90 micro-physical cloud processes and radiative transfer (Ritter and Geleyn, 1992) into account. COSMO-CLM has proven to
be an adequate tool for long-term convection-permitting simulations, allowing for a statistical analysis of mesoscale weather
systems (Brisson et al., 2016; Thiery et al., 2015; Van de Walle et al., 2020). It has also shown its value for studying wind speed
metrics (Nolan et al., 2014; Wiese et al., 2019; Akhtar et al., 2021; Petrik et al., 2021). The model is directly driven by the
31 km resolution ERA5 reanalysis data (Hersbach et al., 2018). More information about the nesting strategy can be found in
95 appendix A. Some deficiencies in ERA5, like meridional variability of surface winds, and moist convection (Belmonte Rivas
and Stoffelen, 2019) are better represented at the kilometre scale resolution. ERA5 wind speeds have a general accuracy of
about 1.0 m/s (Vogelzang and Stoffelen, 2021). To account for the relaxation and spin up of the forcing data 20 grid points
from every side of the domain are excluded from the analysis domain. The setup for this simulation has been used before to
investigate the effect of wind farms on the regional climate in the German Bight (Chatterjee and van Lipzig, 2020).

2.2 Scatterometer and lidar validation data

The model was evaluated with L3 scatterometer data from the ASCAT instrument on the Metop-A satellite available from the
Copernicus Marine Environment Monitoring Service (CMEMS) (KNMI, 2018). The Metop-A satellite has a Sun-synchronous
orbit and scans the Kattegat at approximately 9h and 21h UTC. The ASCAT instrument from the Metop-A infers the 10-meter
wind vector (J. de Kloe et al., 2017) over sea via the backscatter of the microwave radiation it emits in three different directions.

105   Points flagged by CMEMS for poor quality are removed from the dataset. The scatterometer does not cover the Kattegat on every overpass it makes, yet a total of $299,503$ Wind Vector Cells (WVC) are available for comparison. As the scatterometer only works over water surfaces, it is not available in the vicinity of coastlines (Verhoef et al., 2012). In order to allow for a comparison, the COSMO-model output is aggregated to the 12km grid of the scatterometer data. A deterministic verification of uninitialised model structures, such as the root mean square difference (RMSD) between the two datasets, suffers from a

110   so called double penalty (G. -J. Marseille and A. Stoffelen, 2017). That is why, apart from the RMSD, statistical evaluation methods like the 25th, 50th and 75th percentile wind speeds are also compared.

As a complementary validation to the scatterometer discussed above a light detection and ranging (lidar) device located near the Anholt wind farm is used. This lidar provides 10 minute averages of the wind speed and direction between 2013 and 2014

115   on different height levels, and is offered by Ørsted. The 10 minute averages are compared with the instantaneous wind speeds of the COSMO grid cell corresponding to the location of the lidar. The model wind speeds are interpolated to the measurement height level of the lidar using the wind profile power law given by

$$V(h_{\text{lidar}}) = V(h_m) \cdot \left(\frac{h_{\text{lidar}}}{h_m} \right)^{\alpha}, \tag{1}$$

where the shear coefficient α is given by

120   $$\alpha = \frac{\ln\left(V(h_{m+1})/V(h_m)\right)}{\ln\left(h_{m+1}/h_m\right)}. \tag{2}$$

Here h_{lidar}, h_m and h_{m+1} are measurement height of the lidar, and the two COSMO output levels closest to the measurement height of the lidar. The agreement between the lidar data and the model output is quantified using the Perkins Skill Score (PSS) (Perkins et al., 2007). The PSS quantifies the overlap between two equally-binned probability distributions, and is calculated by taking the sum of the minimum of the two probability distributions over all the bins. Formally this is expressed as

125   $$\text{PSS} = \sum_{i=1}^{N_{\text{bins}}} \min\left(\text{lidar}_i, \text{model}_i\right), \tag{3}$$

with lidar_i and model_i being the bin values of respectively the lidar and the model probability distributions.

2.3   Metrics for temporal variations in wind speed

The spectral density of a signal is estimated using a periodogram calculated with the Welch method (Welch, 1967). Due to the uncertainty in a signal such as a time series of the wind speed, we can only make an estimation of the underlying spectrum. In

130   the Welch method the 10-year time series of 10-minute interval wind speeds is cut in overlapping sections of approximately seven days (1024 output intervals) in our case, with an overlap of 50%. Subsequently the spectral density of every section is calculated using a Fast Fourier Transform (FFT) algorithm. In order to reduce the reflections arising from performing an FFT on a finite time series, a Hann window is used to cut the signal into sections (Blackman and Tukey, 1958). The final mean spectrum is then calculated as the average of the spectrum of every section. This last step averages out the fast natural

135 variability of the spectrum and results in a good estimate for the true 10-year mean spectral density of the signal.

The periodogram is calculated for the four meteorological seasons, each integrated over a 3-month interval, allowing for a comparison between different seasons. The typical periodogram for a certain season (for instance spring, comprising the months March, April and May) is then obtained by taking the mean of the periodogram of that season over every year of the

140 simulation (in this example taking the mean over all the spring periods in the years 2010-2019). For the winters of 2010 and 2019 the months December and the months January & February are respectively not included in the spectrum. Calculating the combined periodogram of these disjunct time periods is useful to depict the seasonal effect in wind variability. A Student's-t test on the 95% confidence level is used to quantify if the differences between the winter and the summer spectra are significant over a given period.

145

With the method described above an average periodogram of the 100 meter wind speed is calculated for every grid point for every season. These averaged periodograms can be integrated over a time interval of interest resulting in one single value per grid point that quantifies the temporal variability over that time interval for every season, making it possible to visually compare the different grid points for each season.

150

Periodograms can also be used to examine the fluctuations in potential wind power. The powercurve of a wind turbine converts a wind speed time series to a wind power time series, and of the latter time series a periodogram can be calculated. The powercurve of the Siemens SWT-3.6-120 wind turbine is available in table form (Bauer and Matysik, 2022), and a cubic spline interpolation is used to obtain the power for every possible wind speed.

155 **2.4 Metrics for spatial variations in wind speed**

We introduce the Mesoscale Spatial Variability Index (MSVI), extracted from the horizontal wind field at 100 meter, by sliding two square windows of different sizes grid point by grid point over the study area (fig. 2). Within both of these windows the mean wind speed is calculated. The small window aims to estimate the mesoscale wind speed, while the large window follows more or less the synoptic background. The MSVI is defined as the deviation of the ratio between these two wind speeds with

160 one:

$$\text{MSVI} = \frac{\langle v \rangle_{\text{small window}}}{\langle v \rangle_{\text{large window}}} - 1 \tag{4}$$

and returns a dimensionless number quantifying how much larger mesoscale wind speeds are relative to the synoptic background.

165 The size of the small window is defined by the effective resolution of the simulation, which is approximately 10×10 grid points (Kapper et al., 2010) ($\sim 15\,\text{km}$). The size of the large window is nine times larger in area than the small window in order to have enough contrast between the two means, but is still smaller than the length scales of the synoptic systems so that
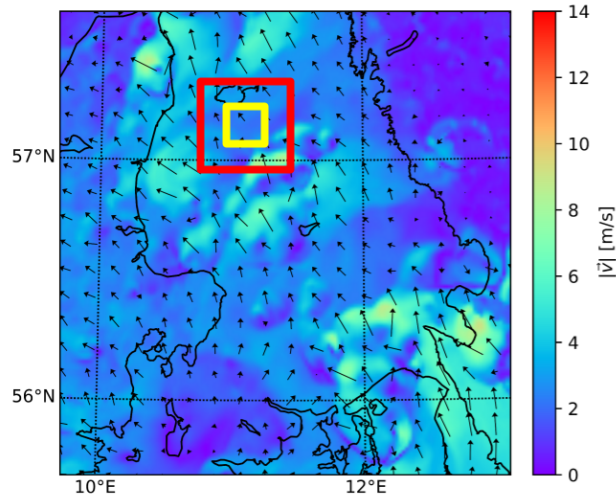
Figure 2. Wind speed and direction at 100 metres. The squares illustrate the windows defined for the Mesoscale Spatial Variability Index (MSVI) calculation. For this (and every other) hourly time step, both windows slide over the whole simulation domain and the maximum MSVI is saved.

it can sufficiently follow these trends. Therefore, a size of 30 grid points (~ 45 km) is chosen for the large window size. As the large window comprises the small window, an upper bound exists for the metric. Indeed: when the small window has a mean wind speed of x m/s, and the large window has a wind speed of 0 m/s everywhere, but in the small window, the denominator of the MSVI will be $\frac{1}{9} \cdot x$ m/s, giving an upper bound of eight to the MSVI.

Since the focus of this paper is on the offshore wind conditions, the MSVI is calculated only if at least 75% of the large window is sea, while all the onshore wind speed values are set to NaN. The maximum value per time step is calculated, quantifying the intensity of a mesoscale weather system in the domain during that specific time step.

Given the offshore wind speed variability, wind power fluctuations are expected. Wind speed and wind power are related to each other via the power curve of a wind turbine, and given this relation an attempt at an MSVI analysis on the wind power could be made. Yet the shape of this power curve imposes restrictions on our methodology: bellow the cut-in wind speed of a turbine (3 m/s) no power is produced, prohibiting a MSVI calculation for power fluctuations as the denominator would become zero. Instead we opt for a RMSD comparison between power time series for a stationary 10×10 window and a 30×30 window. The stationary windows are positioned in the area of the Anholt wind farm. The small window is in area nine times smaller than the large window. In order to cover the whole large window, nine small window power time series are calculated and compared to the large window power time series. The average over these nine RMSD values is then taken to assess the differences in wind power.

3   Results

3.1   Evaluation with scatterometer and lidar data

The simulation is evaluated using scatterometer data. Over the 10-year integration we find a spatiotemporal RMSD between the
190   10 m wind speeds of 1.35 m/s, over the data points located away from coastlines and small islands. Note that the ASCAT wind
speed error is about 0.5 m/s (Vogelzang and Stoffelen, 2021) with no particular expected regional deviation in the COSMO
domain (Belmonte Rivas and Stoffelen, 2019). Moreover, the 1.35 m/s RMSD may be explained by the double penalty men-
tioned earlier. However, tests with spectral nudging did not substantially improve the performance indicating that the lateral
boundaries to a large extent control the timing and location of weather systems for this domain and model configuration. Dis-
195   tributions of wind speeds are compared via their 25th, the 50th and the 75th percentiles (fig. 3). For the 25th and to a lesser
extend the 50th percentiles, simulation and observation disagree, especially near the coastlines and over the islands. On the
western shores simulation output and scatterometer agree better than on the eastern shore. The simulation also shows lower
wind speeds over the Anholt and the Læsø islands. Recently, ASCAT winds have been validated extensively close to the coast
and an operational product has been introduced providing good quality winds as close as 10 km from the coast (Vogelzang
200   and Stoffelen, 2022), which could in the future be used to further evaluate the discrepancies between simulation output and
scatterometer data. Relative differences between the simulation and the scatterometer further away from the islands and the
coastline are smaller: -13% for the 25th percentile, +1% for the 50th percentile and +5% for the 75th percentile.

For validation of the model output above the 10 metre level a lidar device measuring the wind speeds at 102.6 metre is
205   used. The 10 minute model wind speeds at the 80 m and 100 m level are extrapolated to 102.6 metre using the wind profile
power law (equation 1) and then compared with the lidar data. The nearby Anholt wind farm was being built during the lidar
measurement campaign. In order to minimise the impact of the Anholt wind farm on the validation of the model, we have also
made a comparison taking only into account the first 100 days of the measurement campaign. During this period the wind farm
availability stayed below 50%. Over the whole 2-year-long lidar data set the normalised PSS of the simulation output compared
210   with the lidar data is 0.97 (fig. 4). During this period the simulation output overestimates the lidar data by on average 0.08 m/s.
Taking only the first 100 days into account results in a similar normalised PSS of 0.96, with COSMO overestimating the lidar
wind speeds by slightly less, namely 0.02 m/s. This implies that the impact of the wind farm on the lidar measurements is
rather small and that the lidar can be used for evaluation purposes of our simulation, which does not take into account the wind
farm.

3.2   Temporal variations

Using the Welch method the spectrum can be estimated for the 10-year 100 meter wind speed time series of each pixel in
our domain. Differences between winter and summer are investigated using the combined periodogram for all winter months
December, January and February (DJF) and for all summer months June, July and August (JJA ; fig. 5). The resulting peri-
odograms resemble what is found in literature by Larsén et al. (2016) for 100 meter offshore wind speed spectra. Comparing
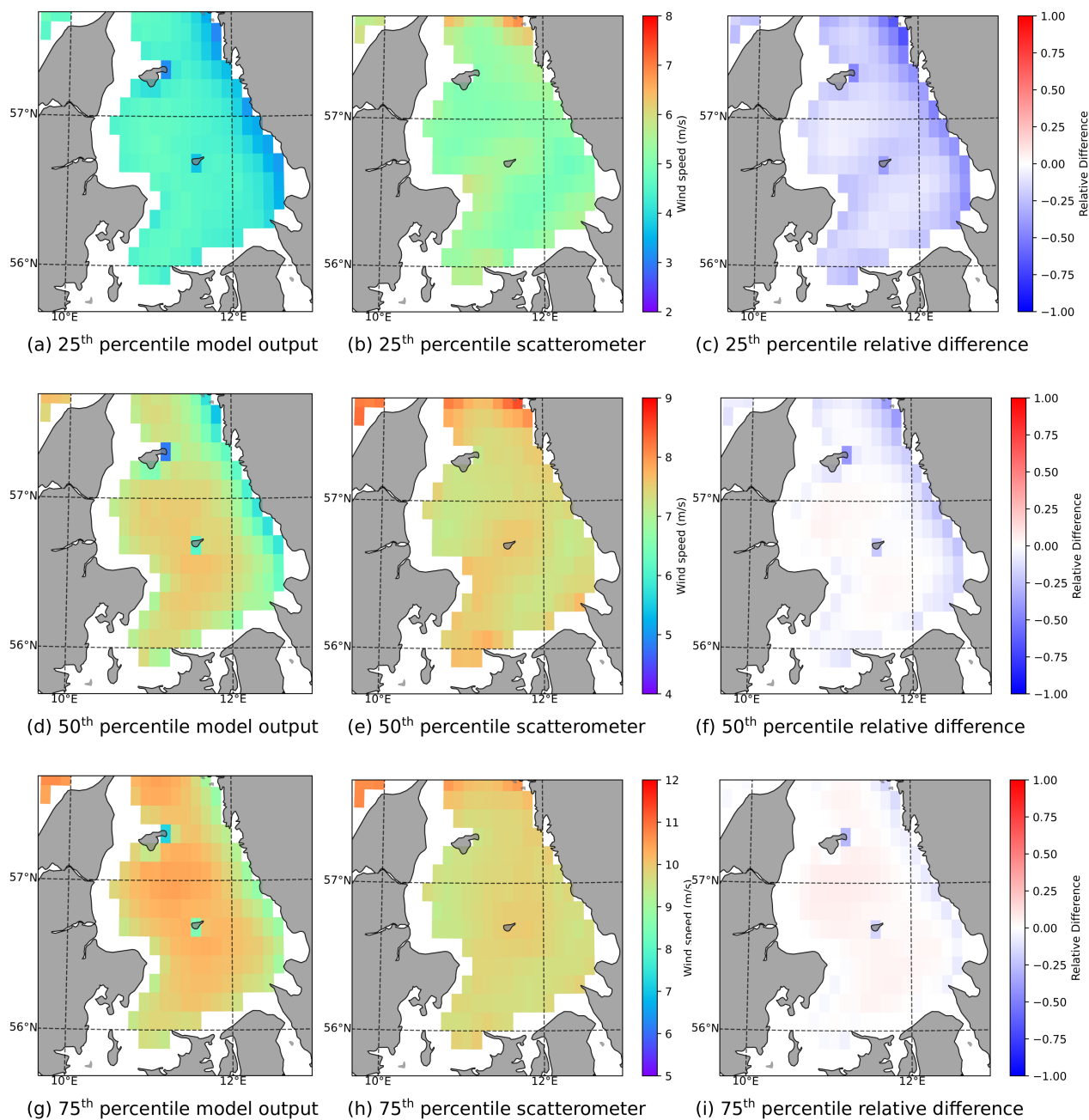
Figure 3. Comparison between the simulation and the scatterometer data. In the right most column the relative differences between the model output and the scatterometer data are plotted (model output - scatterometer data divided by the model). Note the difference in scales between different percentiles.
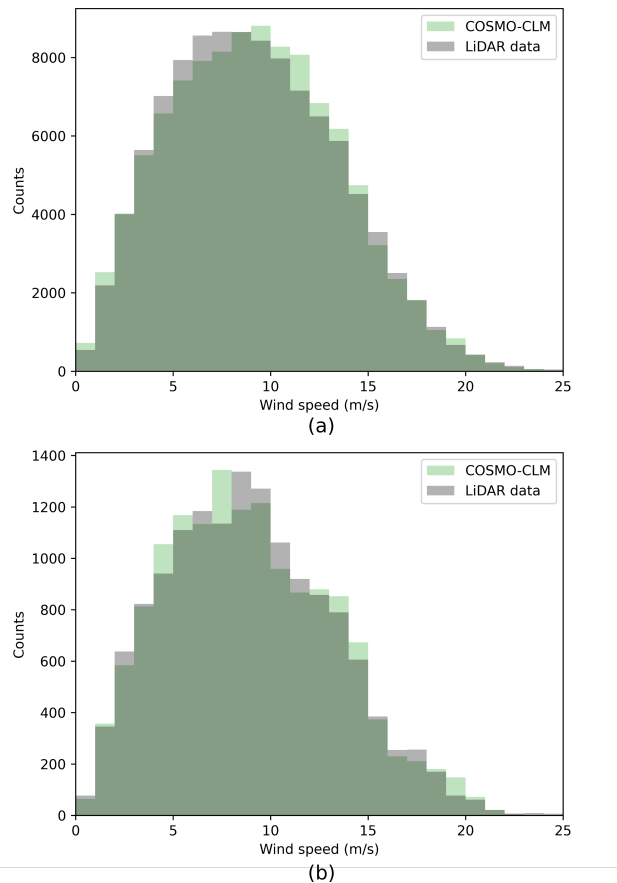
Figure 4. Distributions of both the model and the lidar wind speeds at 10 minute intervals at the position indicated in fig. 1. In **(a)** the whole 2 year measurement period is taken into account, in **(b)** only the first 100 measurement days are used when the wind farm was less than 50% operational.

the simulation output with LiDAR data it appears however that our simulation slightly underestimates the intensity at the higher frequencies. These periodograms are averaged over a subdomain of the Kattegat, excluding coastlines and islands. On the high frequency end of the periodograms, a higher intensity is found in DJF compared to JJA. In winter, the relatively warm seawater creates unstable conditions, which results in larger wind speed variability on the shorter timescales (20min-1h). For wind speed variability on the long timescales (6h-12h), however, there is a larger intensity found for JJA. Using a Student's t-test we find that the differences over these time slots are significant. The difference between DJF and JJA on the longer timescales may be due to the sun being higher in summer, and it heating the land more effectively. With the sun over land, the air above it expands and generates a breeze over the sea during the morning or afternoon. During the night, due to the land cooling nocturnal jets
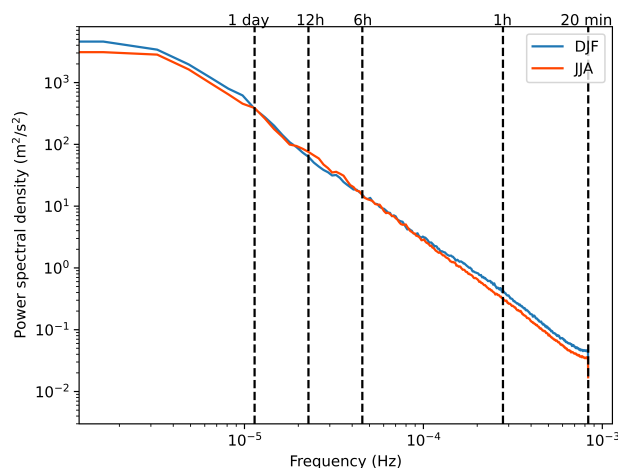
Figure 5. Periodogram of the 100 meter wind speed estimated using the Welch method for both DJF and JJA.

may be formed, which may be advected over the water.

Next, periodograms for each grid cell are integrated over a chosen time slot, resulting in a map that quantifies the wind speed variability, allowing for a spatial analysis of the temporal wind speed variability. In the previous paragraph, a stronger variability was already found in JJA than in DJF for the long timescale winds (fig. 6). In contrast, for the short timescale winds, there is a stronger variability in DJF than in JJA (fig. 6), albeit an order of magnitude weaker than the long timescale variability. During winter the variability increases from southwest to northeast. This gradient is probably related to southwest prevailing winds and indicates that the convective systems need some spin-up time and distance to reach their maximal wind speed variability. Indeed, when isolating a time series of 11 consecutive winter days with only easterly winds (directions from 45° to 135°), a clear gradient is observed from east to west, confirming that spatial spin-up of convective systems is an underlying cause for the large wind speed variability over the northeastern part of the Kattegat. Similarly Vincent et al. (2011) relates wind speed variability over the North Sea in winter on these short timescales to unstable conditions created by the relatively warm sea water and the relatively cold air above. Their higher variability found towards the centre of the North Sea, compared to the coastlines, also indicates the spin-up time needed for the atmospheric conditions to reach maximal variability.

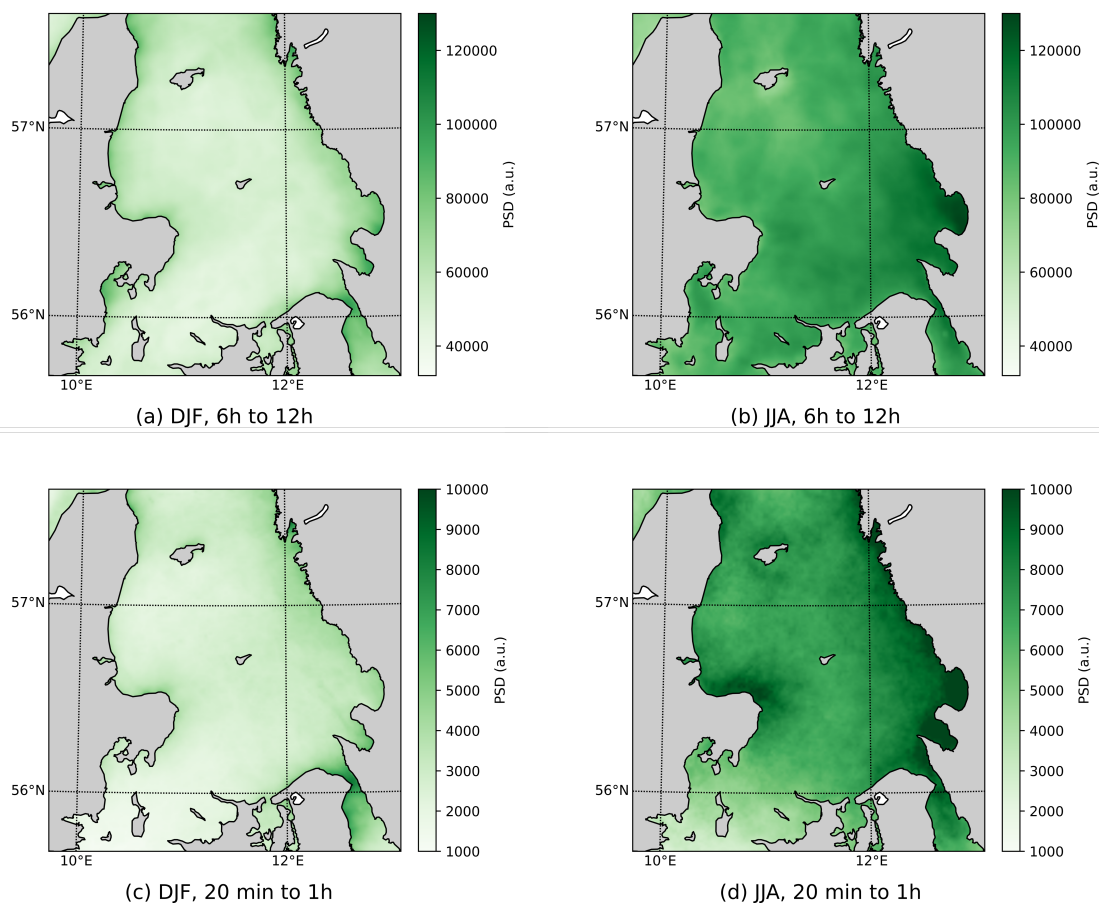### 3.2.1 Integrated periodograms for the potential wind power

The combined periodogram for potential wind power integrated for a time slot running from 6 hours to 12 hours depicts a similar picture as for the wind speed (fig. 6 and fig. 7). Also for potential wind power, the variability is larger in JJA than in DJF. Potential wind power variability on shorter timescales from 20 minutes to one hour, however, differs from wind speed variability: stronger variability is found in summer (compare figs. 6 and 7). The discrepancy between wind speed variability
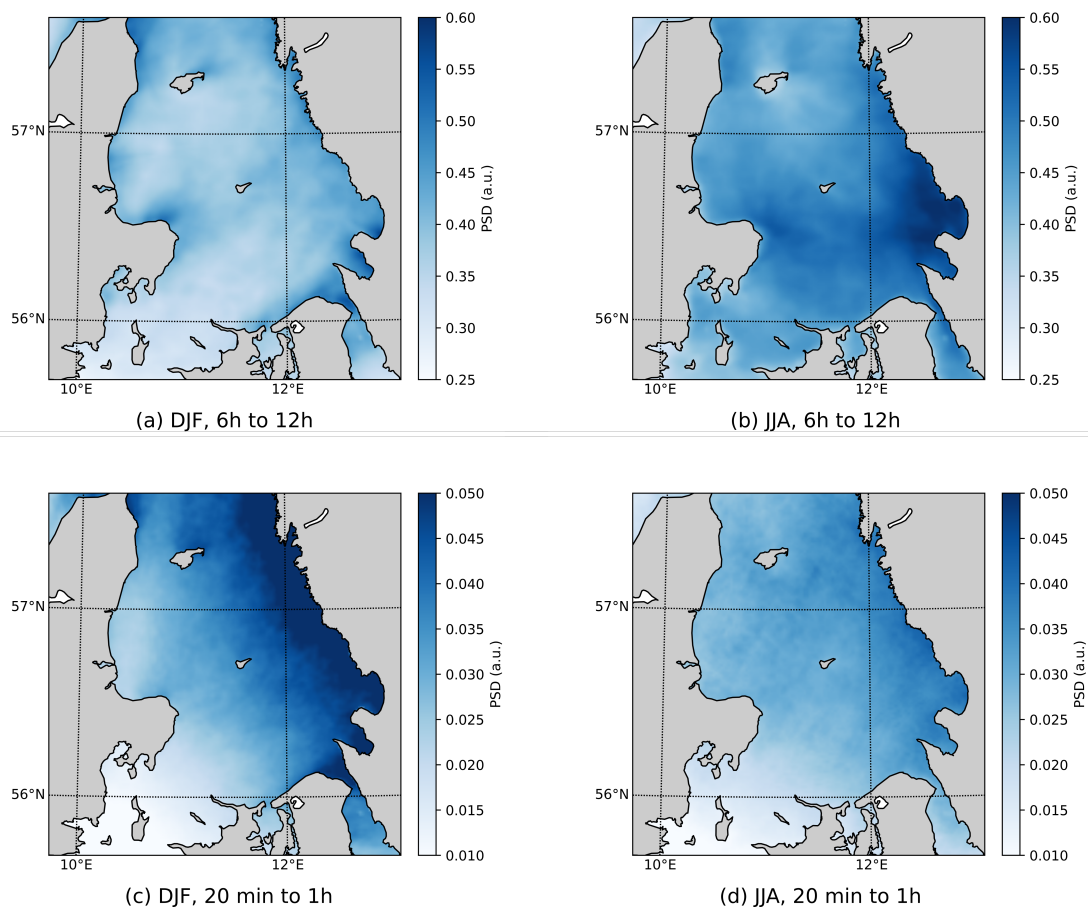
Figure 6. Integrated periodograms for both winter (DJF) as for summer (JJA). **(a, b)** On the long timescales there is a higher intensity in JJA than in DJF. **(c, d)** On the short timescales a higher intensity is found in DJF. This elevated intensity is probably related to convection triggered by the unstable conditions in DJF.

Figure 7. Integrated periodograms of wind power time series for both winter (DJF) as for summer (JJA). **(a, b)** As in figure 6 (a, b) the highest intensity on the long timescales is found in JJA. **(c, d)** Contrary to figure 6 (c, d) the larger variations in potential wind power are found here in JJA, while the larger fluctuations in wind speed on these timescales are found in DJF.
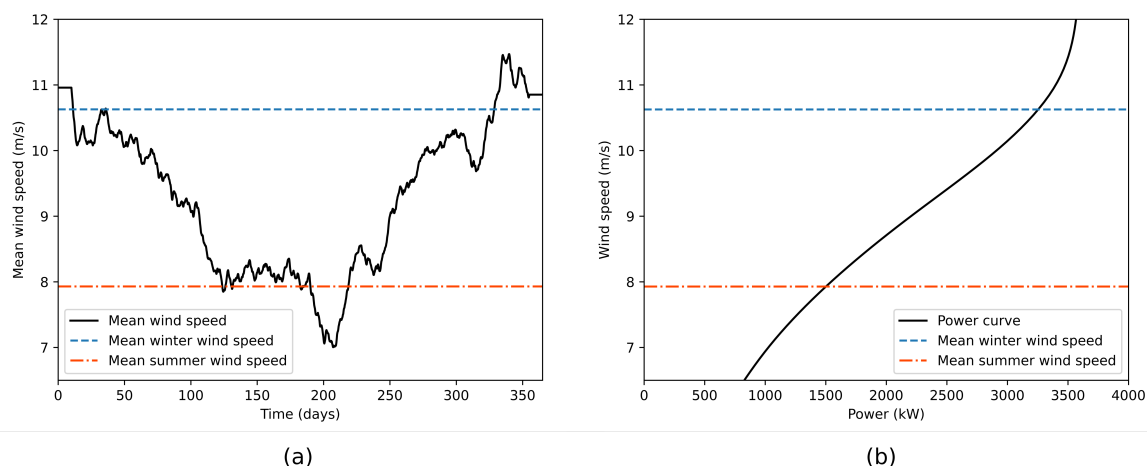
Figure 8. (**a**) Yearly mean 100 m wind speed over the Kattegat and (**b**) the power curve of the Anholt wind farm turbines. The power curve of a wind turbine relates a wind speed to a power output for that wind turbine.
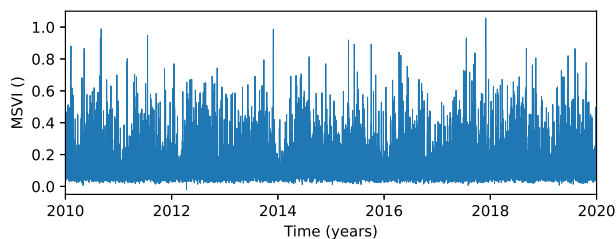

Figure 9. Time series of the mesoscale spatial variability index for the ten year model integration.

and potential wind power variability is due to the particular shape of the power curve. This can be explained using the yearly mean wind speed and the power curve of the wind turbine used in this example (fig. 8). In winter, wind speeds are comparable

250 to the rated wind speed of the turbine. Between the rated wind speed and the cut-out wind speed the power output of the turbine stays constant, so fluctuations around this speed do not result in fluctuations in the potential wind power. In summer, the mean wind speed is lower and closer to the regime where the potential wind power is proportional to the cube of the wind speed, resulting in large fluctuations in potential wind power. On the shorter timescales fluctuations in wind speeds thus do not necessarily translate to fluctuations in potential wind power.

255 **3.3 Spatial variations in wind speed**

The time series of the maximum MSVI features some peaks (fig. 9) resulting from mesoscale systems causing wind speed variability. Indeed, looking at the wind fields associated with these peaks, a variety of mesoscale systems are clear, such as
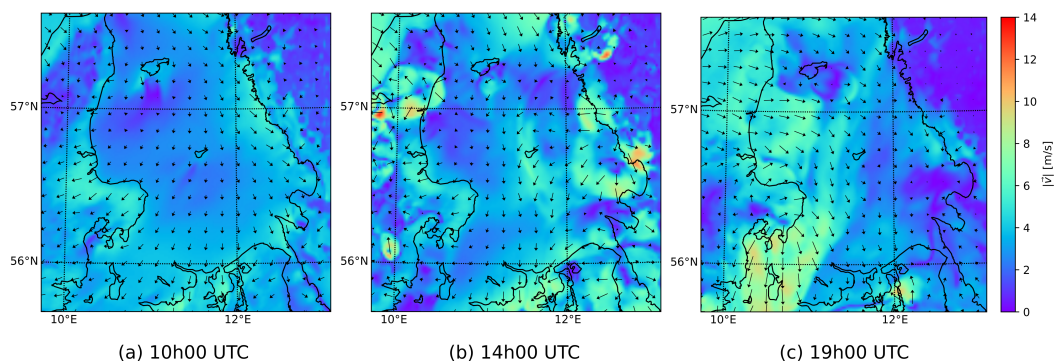
Figure 10. 100m wind speed of a convective system travelling over the Kattegat on June 6, 2014. The system is accompanied by local showers. A movie of this system is provided in Supplementary material 1.
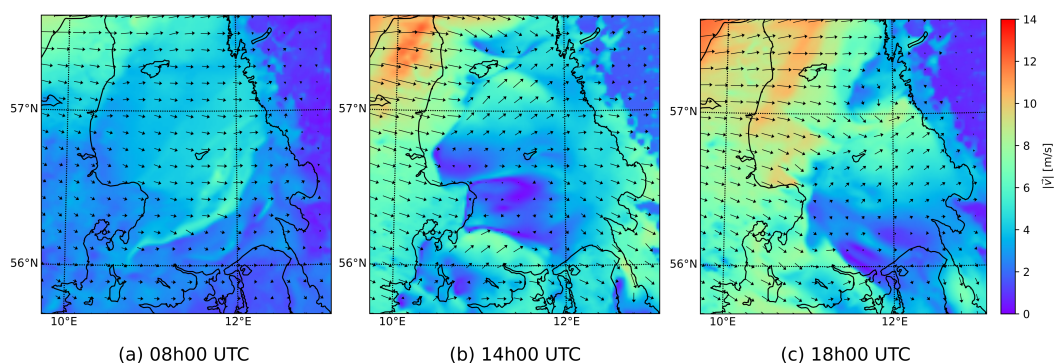
Figure 11. 100m wind speed of a sea breeze system over the Kattegat on August 28, 2013. While there is no onshore front, the system still affects the wind speeds over the Kattegat. A movie of this system is provided in Supplementary material 2.

convective and sea breeze systems developing over the Kattegat. Convective cells are initiated over land and the Læsø island in the afternoon, resulting in local showers and offshore wind speed variability (fig. 10) . Other peaks relate to sea breeze systems also causing spatial wind speed variability (fig. 11). In the case study, no onshore front is formed due to strong synoptic winds. However, this system still has a large impact on offshore winds, with a substantial drop in wind speed where the sea breeze counteracts the synoptic flow. At sunset the sea breeze systems detach and the synoptic wind over the Kattegat recovers. Convective and the sea breeze systems are quite different, yet they both create mesoscale wind speed variations quantified by the MSVI.

Both the mean MSVI and its diurnal amplitude is higher in summer (JJA) than winter (DJF) (fig. 12). In winter, wind speed variability is more or less constant throughout the day. In summer the MSVI clearly peaks in the afternoon, when the surface temperature over land reaches its maximum, confirming an influence of the land on the mesoscale winds over sea. Over at least one area over sea the mesoscale wind speed is on average 20% larger than the synoptic wind speed at 17h UTC in summer.

260

265

270 Moreover, when analysing individual cases with a high mesoscale wind speed component, it can be seen that the systems detected in summer often originate over land and then travel over sea. Models that explicitly resolve convection feature more mesoscale spatial variability in wind speed compared to coarser model data sets as for example the ERA5 reanalysis. Calculating the mean MSVI for ERA5 over our simulation domain results in a substantially lower MSVI, and a smaller diurnal amplitude. To confirm that this is indeed the inability of a coarser scale gridded model to resolve mesoscale variability we have

275 conservatively remapped the output of our convection permitting COSMO simulation to the ERA5 grid and then calculated the MSVI, which also resulted in a substantially smaller MSVI than the original simulation. The difference between the coarser scale COSMO MSVI and the ERA5 MSVI on the same resolution might be due to the fact that the effective resolution of a model is substantially coarser than the native resolution. By aggregating to a coarser scale still part of the advantage of a high resolution model remains as earlier demonstrated by Brisson et al. (2016) for precipitation in convection permitting simulations.

280

The power output over the ten year simulation period is comparable for the small and the large window time series. The additional wind speed variations that the small windows capture cancel out over the simulation duration. The RMSD between the nine small windows on the one hand and the large window on the other hand is however quite substantial. At 286 kW this is 14% of the average power output. The wind speed variability captured by the mesoscale window translates to a non-trivial

285 portion of the wind power variability. Therefore accurate forecasting of power fluctuations requires accurate high resolution wind forecasts.

4 Conclusions

We have established a convection-permitting simulation over the Kattegat area to investigate the mesoscale variability of offshore conditions and its influence on wind power fluctuations. The simulation showed good agreement with scatterometer

290 observations away from coasts and small islands with a spatiotemporal root mean square difference of 1.35 m/s. As scatterometer products become more and more accurate near coastlines (Vogelzang and Stoffelen, 2022), future research will be able to study the nature of the discrepancies between simulation output and scatterometer data. Also at the 100-metre level, the 10-minute wind speed over the 2 years of available lidar data were well represented by the COSMO simulation. The bias is 0.08 m/s and the PSS, which is the overlap between the lidar and COSMO wind speed probability distributions, is 0.97.

295

The temporal variability was quantified over different timescales by integrating the Welch spectrum. Our results show that more variability in wind speed is expected in winter due to unstable conditions over sea. These unstable offshore conditions result in wind speed variability on short timescales (20 minutes to 1 hour), resulting from propagating convective systems spinning up over the relatively warm sea. The maximum variability is found in the northeastern part of the Kattegat, since

300 southwesterly winds are prevailing. The variability on long timescales (6 hours to 12 hours) is found more pronounced in summer than in winter, probably due to the development of sea breeze systems.
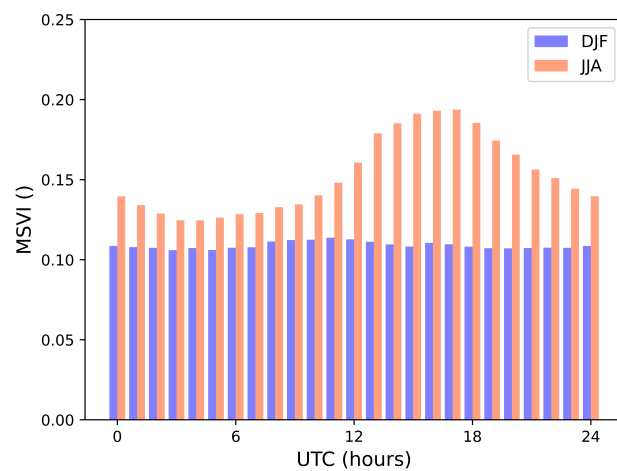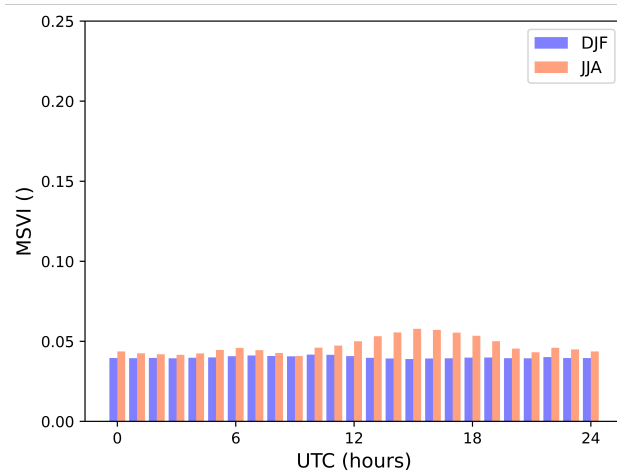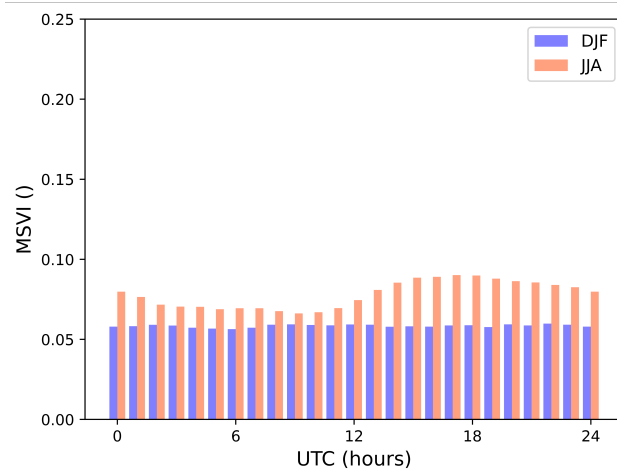
Figure 12. Hourly distribution of the MSVI for both winter (DJF) and summer (JJA). **(a)** MSVI of the high resolution COSMO simulation output. **(b)** MSVI of the ERA5 reanalysis data. **(c)** MSVI of the COSMO simulation output regridded to the ERA5 grid.

The power curve of an offshore wind turbine converts the wind speed data to power output data which, opposite to wind speed fluctuations, show that the energy production is more subject to fluctuations in summer than in winter. In summer the mean wind speed is situated in a regime where power output is very sensitive to wind speed fluctuation. In winter the mean wind speed is closer to the rated wind speed of a turbine, where the mean power output is less sensitive to wind speed fluctuations.

The offshore mesoscale spatial variability was studied using the MSVI defined in section 2. The MSVI is the deviation of ratio between the mean wind speed in a small window and a large window from one, calculated for every offshore position in the domain. The maximum MSVI in the Kattegat per time step is used to study the mesoscale wind speed variability. On average over a 10 year period the mesoscale wind speed in the Kattegat is up to 20% larger than the synoptic wind speed at 17h UTC during summer, exhibiting a clear diurnal cycle of systems forming over land transported over sea. Coarser grid models, as for instance ERA5, do not capture this variability and subsequently underestimate the MSVI. Spatial scales of modern large wind farms and mesoscale weather systems are similar, therefore the whole power grid becomes subject to power production fluctuations of a single farm. Though mesoscale climate modelling at the kilometre scale does not improve the mean power production estimation for the Kattegat, it is essential to correctly represent substantial power production fluctuations. The same argumentation is valid for resource assessment and climate change projections. Although mean power production might be well represented at the 30 km scale, yet models at the km scale are needed to gain insight in the variability at the hourly timescales.

The methods used in this paper can be applied to other regions. Research by Grams et al. (2017) has shown the importance of diversifying the deployment regions for wind energy in order to provide a stable electricity supply. Regions such as for example the Baltic Sea and the Mediterranean will become important to fill the gaps in the wind energy supply. Since most of the Mediterranean is not suited for fixed foundation wind turbines, this area has hardly been exploited for offshore wind energy. Further developments in floating wind turbines, which can operate at larger depths, could open up many opportunities for the Mediterranean, and other deep seas surrounded by complex coastlines.

Author contributions. Jérôme Neirynck contributed to the conceptualisation and methodology, the curating of data, the analysis of the data, the project administration, the visualisation and the writing of the paper. Jonas Van de Walle contributed to the methodology and simulation

setup, the interpretation of the data, the visualisation and the writing of the paper. Ruben Borgers and Sebastiaan Jamaer contributed to the
335   methodology, the interpretation of the data and the writing of the paper. Johan Meyers contributed to the conceptualisation and methodology,
the data collection, the interpretation and discussion of the data, and the writing of the paper. Ad Stoffelen contributed to the methodology,
the data collection, the interpretation and discussion of the data and the writing of the paper. Nicole van Lipzig contributed to the conceptu-
alisation of the study, the methodology, the data collection and interpretation, the overall supervision of the research project, and the writing
of the paper.

340   *Competing interests.*   One of the co-authors, Johan Meyers, is an associate editor of the WES journal. The authors have no other competing
interests to declare.

Appendix A: Nesting strategy

Nesting strategies for regional climate modelling at the kilometre scale can vary greatly from model to model (Prein et al.,
2015). Many studies use a 1:10 resolution jump, but a 1:20 resolution jump has been done before. In previous work that we did
350   with COSMO-CLM, a clear benefit was found in the representation of mesoscale weather systems by directly nesting within a
25 km grid spacing host domain to 2.8 km, instead of using nesting steps in between (Brisson et al., 2015).

Different simulation setups have been tested for 3 month integrations. These tests included different domains (340×360
grid points compared to 180×184 grid points), adding an intermediate nesting at ≈ 12 km resolution and applying spectral
355   nudging. We found no added value of using a larger domain, of adding an in between nesting step and of applying spectral
nudging compared to the wind data from scatterometer. This result is in line with the findings of Ban et al. (2021) where differ-
ent nesting strategies of COSMO-CLM in ERA-Interim do not show any substantial differences. For the temporal mesoscale
variance metric as defined by Vincent and Hahmann (2015) we found that the larger domain appears to have a slightly higher
variance, but the difference between both simulations is rather small.

360

For the assessment of the mesoscale variance in our simulation we analysed the spectra of the LiDAR and the simulation
100 m wind speeds (fig A1). The dashed lines represent the timescales used to define the mesoscale variance in Vincent
and Hahmann (2015). Over these timescales simulation and results appear to agree quite well, even though near the higher
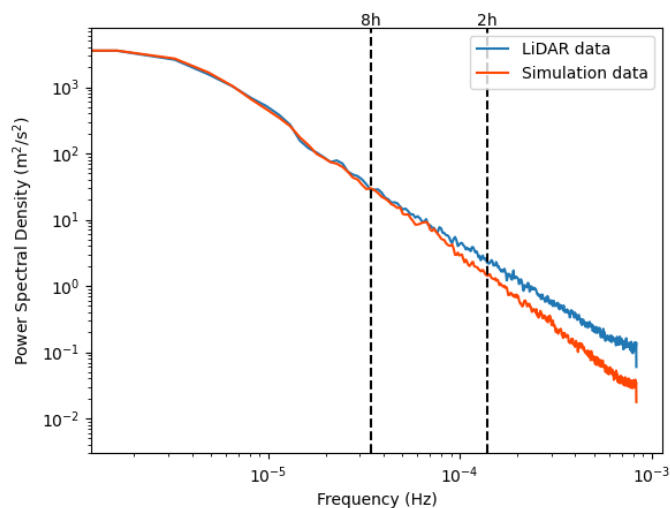
Figure A1. Spectra for the LiDAR and simulation 100 m wind speeds.
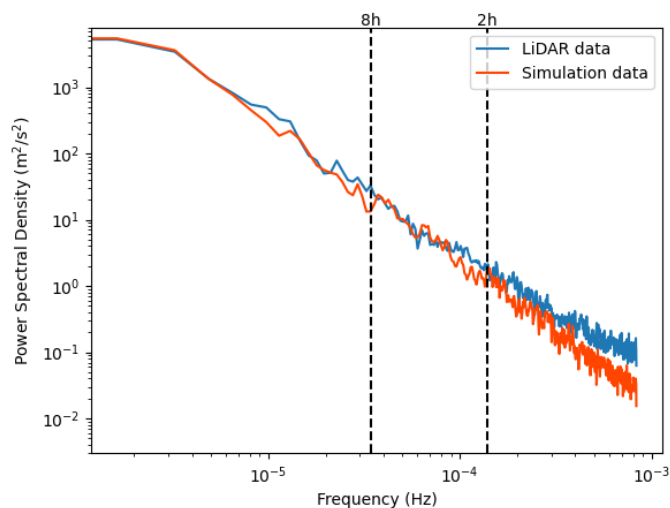
Figure A2. Spectra for the LiDAR and simulation 100 m wind speeds for the first 100 measurement days, when the Anholt wind farm was less than 50% operational.

frequencies the spectra start to diverge. For the first 100 measurement days (fig A2) the agreement seems to be better, but due

365   to natural variability not being averaged out in this relatively small dataset uncertainties become larger.

References

Ahrens, C. D. (1994), *Meteorology Today: an introduction to weather, climate and the environment*, West Publishing company.

Akhtar, N., Geyer, B., Rockel, B., Sommer, P. S. and Schrum, C. (2021), 'Accelerating deployment of offshore wind energy alter wind climate and reduce future power generation potentials', *Scientific reports* **11**(1), 1–12.

Ban, N., Caillaud, C., Coppola, E., Pichelli, E., Sobolowski, S., Adinolfi, M., Ahrens, B., Alias, A., Anders, I., Bastin, S. et al. (2021), 'The first multi-model ensemble of regional climate simulations at kilometer-scale resolution, part i: evaluation of precipitation', *Climate Dynamics* **57**, 275–302.

Batchelor, G. K. (2000), *An introduction to fluid dynamics*, Cambridge university press.

Bauer, L. and Matysik, S. (2022), 'Datasheet of the siemens swt-3.6-120 wind turbine'. Available from https://en.wind-turbine-models.com/turbines/646-siemens-swt-3.6-120-onshore, Accessed: 2022-07-11.

Belmonte Rivas, M. and Stoffelen, A. (2019), 'Characterizing ERA-interim and ERA5 surface wind biases using ASCAT', **15**(3), 831–852.
URL: *https://os.copernicus.org/articles/15/831/2019/*

Betakova, V., Vojar, J. and Sklenicka, P. (2015), 'Wind turbines location: How many and how far?', *Applied Energy* **151**, 23–31.

Blackman, R. B. and Tukey, J. W. (1958), 'The measurement of power spectra from the point of view of communications engineering—part i', *Bell System Technical Journal* **37**(1), 185–282.

Bolgiani, P., Calvo-Sancho, C., Díaz-Fernández, J., Quitián-Hernández, L., Sastre, M., Santos-Muñoz, D., Farrán, J., González-Alemán, J. J., Valero, F. and Martín, M. (2022), 'Wind kinetic energy climatology and effective resolution for the era5 reanalysis', *Climate Dynamics* **59**(3-4), 737–752.

Brisson, E., Demuzere, M. and Van Lipzig, N. (2015), 'Modelling strategies for performing convection-permitting climate simulations', *Meteorologische Zeitschrift* **25**(2), 149–163.

Brisson, E., Van Weverberg, K., Demuzere, M., Devis, A., Saeed, S., Stengel, M. and van Lipzig, N. P. (2016), 'How well can a convection-permitting climate model reproduce decadal statistics of precipitation, temperature and cloud characteristics?', *Climate Dynamics* **47**(9), 3043–3061.

Calaf, M., Meneveau, C. and Meyers, J. (2010), 'Large eddy simulation study of fully developed wind-turbine array boundary layers', *Physics of fluids* **22**(1), 015110.

Carvalho, D., Rocha, A., Gómez-Gesteira, M. and Santos, C. S. (2014), 'Wrf wind simulation and wind energy production estimates forced by different reanalyses: Comparison with observed data for portugal', *Applied Energy* **117**, 116–126.

Chatterjee, F. and van Lipzig, N. (2020), Wind farm impacts on the regional climate of the German Bight. A regional climate model study, PhD thesis, KU Leuven, Department of Earth and Environmental Sciences.

Chung, T. et al. (2002), *Computational fluid dynamics*, Cambridge university press.

Díaz, H. and Soares, C. G. (2020), 'Review of the current status, technology and future trends of offshore wind farms', *Ocean Engineering* **209**, 107381.

Doms, G. and Baldauf, M. (2018), 'A description of the nonhydrostatic regional cosmo-model part i: dynamics and numerics', *Deutscher Wetterdienst, Offenbach* . cosmo-model.org.

G. -J. Marseille and A. Stoffelen (2017), 'Toward scatterometer winds assimilation in the mesoscale HARMONIE model', **10**(5), 2383–2393.

Grams, C. M., Beerli, R., Pfenninger, S., Staffell, I. and Wernli, H. (2017), 'Balancing europe's wind-power output through spatial deployment informed by weather regimes', *Nature climate change* **7**(8), 557–562.

Helsen, S., van Lipzig, N. P., Demuzere, M., Vanden Broucke, S., Caluwaerts, S., De Cruz, L., De Troch, R., Hamdi, R., Termonia, P., Van Schaeybroeck, B. et al. (2020), 'Consistent scale-dependency of future increases in hourly extreme precipitation in two convection-permitting climate models', *Climate Dynamics* **54**(3), 1267–1280.

Hersbach, H., Bell, B., Berrisford, P., Biavati, G., Horányi, A. et al. (2018), 'Era5 hourly data on pressure levels from 1979 to present', *Copernicus Climate Change Service (C3S) Climate Data Store (CDS)* **10**. Accessed at DKRZ.

Hossain, J. and Pota, H. R. (2014), Robust control for grid voltage stability: High penetration of renewable energy, *in* 'Power systems', Springer.

J. de Kloe, A. Stoffelen and A. Verhoef (2017), 'Improved use of scatterometer measurements by using stress-equivalent reference winds', **10**(5), 2340–2347.

Jankov, I., Gallus, W. A., Segal, M., Shaw, B. and Koch, S. E. (2005), 'The impact of different wrf model physical parameterizations and their interactions on warm season mcs rainfall', *Weather and forecasting* **20**(6), 1048–1060.

Kaldellis, J. and Kapsali, M. (2013), 'Shifting towards offshore wind energy—recent activity and future development', *Energy policy* **53**, 136–148.

Kapper, K. L., Truhetz, H. and Gobiet, A. (2010), Determination of the effective resolution of regional climate models, *in* 'EGU General Assembly Conference Abstracts', p. 10479.

Kempton, W., Pimenta, F. M., Veron, D. E. and Colle, B. A. (2010), 'Electric power from offshore wind via synoptic-scale interconnection', *Proceedings of the National Academy of Sciences* **107**(16), 7240–7245.

KNMI (2018), 'Global ocean daily gridded reprocessed l3 sea surface winds from scatterometer'. Available from: http://marine.copernicus.eu/services-portfolio/access-to-products/?option=com_csw&view=details&product_id=WIND_GLO_WIND_L3_REP_OBSERVATIONS_012_005.

Lanzilao, L. and Meyers, J. (2022), Effects of self-induced gravity waves on finite wind-farm operations using a large-eddy simulation framework, *in* 'Journal of Physics: Conference Series', Vol. 2265, IOP Publishing, p. 022043.

Larsén, X. G. and Fischereit, J. (2021), 'A case study of wind farm effects using two wake parameterizations in the weather research and forecasting (wrf) model (v3. 7.1) in the presence of low-level jets', *Geoscientific Model Development* **14**(6), 3141–3158.

Larsén, X. G., Larsen, S. E. and Petersen, E. L. (2016), 'Full-scale spectrum of boundary-layer winds', *Boundary-layer meteorology* **159**(2), 349–371.

Meyers, J. and Meneveau, C. (2012), 'Optimal turbine spacing in fully developed wind farm boundary layers', *Wind energy* **15**(2), 305–317.

Milborrow, D. (2020), Wind energy economics, *in* 'The Age of Wind Energy', Springer, pp. 307–326.

Molina, M. O., Gutiérrez, C. and Sánchez, E. (2021), 'Comparison of era5 surface wind speed climatologies over europe with observations from the hadisd dataset', *International Journal of Climatology* **41**(10), 4864–4878.

Müller, S., Larsén, X. G. and Verelst, D. (2023), 'Tropical cyclone low-level wind speed, shear, and veer: sensitivity to the boundary layer parameterization in wrf', *Wind Energy Science Discussions* **2023**, 1–23.

Nolan, P., Lynch, P. and Sweeney, C. (2014), 'Simulating the future wind energy resource of ireland using the cosmo-clm model', *Wind Energy* **17**(1), 19–37.

Nunalee, C. G. and Basu, S. (2014), 'Mesoscale modeling of coastal low-level jets: implications for offshore wind resource estimation', *Wind Energy* **17**(8), 1199–1216.

Olauson, J. (2018), 'Era5: The new champion of wind power modelling?', *Renewable energy* **126**, 322–331.

440   Orlanski, I. (1975), 'A rational subdivision of scales for atmospheric processes', *Bulletin of the American Meteorological Society* pp. 527–530.

Peña, A., Schaldemose Hansen, K., Ott, S. and van der Laan, M. P. (2018), 'On wake modeling, wind-farm gradients, and aep predictions at the anholt wind farm', *Wind Energy Science* **3**(1), 191–202.

Perkins, S., Pitman, A., Holbrook, N. and McAneney, J. (2007), 'Evaluation of the ar4 climate models' simulated daily maximum tempera-
445   ture, minimum temperature, and precipitation over australia using probability density functions', *Journal of climate* **20**(17), 4356–4376.

Petrik, R., Geyer, B. and Rockel, B. (2021), 'On the diurnal cycle and variability of winds in the lower planetary boundary layer: evaluation of regional reanalyses and hindcasts', *Tellus A: Dynamic Meteorology and Oceanography* **73**(1), 1–28.

Porchetta, S., Temel, O., Warner, J. C., Muñoz-Esparza, D., Monbaliu, J., van Beeck, J. and van Lipzig, N. (2021), 'Evaluation of a rough-
ness length parametrization accounting for wind–wave alignment in a coupled atmosphere-wave model', *Quarterly Journal of the Royal*
450   *Meteorological Society* **147**(735), 825–846.

Prein, A. F., Langhans, W., Fosser, G., Ferrone, A., Ban, N., Goergen, K., Keller, M., Tölle, M., Gutjahr, O., Feser, F. et al. (2015), 'A review on regional convection-permitting climate modeling: Demonstrations, prospects, and challenges', *Reviews of geophysics* **53**(2), 323–361.

Raschendorfer, M. (2001), 'The new turbulence parameterization of lm', *COSMO newsletter* **1**, 89–97.

Ritter, B. and Geleyn, J.-F. (1992), 'A comprehensive radiation scheme for numerical weather prediction models with potential applications
455   in climate simulations', *Monthly weather review* **120**(2), 303–325.

Rockel, B., Will, A. and Hense, A. (2008), 'The regional climate model cosmo-clm (cclm)', *Meteorologische Zeitschrift* **17**(4), 347–348.

Schulz, J.-P. (2008*a*), 'Introducing sub-grid scale orographic effects in the cosmo model', *COSMO Newsletter* **9**, 29–36.

Schulz, J.-P. (2008*b*), 'Revision of the turbulent gust diagnostics in the cosmo model', *COSMO Newsletter* **8**, 17–22.

Shukla, P., Skea, J., Slade, R., Al Khourdajie, A., van Diemen, R., McCollum, D., Pathak, M., Some, S., Vyas, P., Fradera, R., Belkacemi, M.,
460   Hasija, A., Lisboa, G., Luz, S., Malley, J. and (eds.) (2022), 'Climate change 2022: Mitigation of climate change. contribution of working group iii to the sixth assessment report of the intergovernmental panel on climate change', *Cambridge University Press, Cambridge, UK and New York, NY, USA*. .

Skamarock, W. C. (2004), 'Evaluating mesoscale nwp models using kinetic energy spectra', *Monthly weather review* **132**(12), 3019–3032.

Steele, C., Dorling, S., von Glasow, R. and Bacon, J. (2015), 'Modelling sea-breeze climatologies and interactions on coasts in the southern
465   north sea: implications for offshore wind energy', *Quarterly Journal of the Royal Meteorological Society* **141**(690), 1821–1835.

Thiery, W., Davin, E. L., Panitz, H.-J., Demuzere, M., Lhermitte, S. and van Lipzig, N. P. (2015), 'The impact of the african great lakes on the regional climate', *Journal of Climate* **28**(10), 4061–4085.

Tiedtke, M. (1989), 'A comprehensive mass flux scheme for cumulus parameterization in large-scale models', *Monthly weather review* **117**(8), 1779–1800.

470   Van de Walle, J., Thiery, W., Brousse, O., Souverijns, N., Demuzere, M. and van Lipzig, N. P. (2020), 'A convection-permitting model for the lake victoria basin: Evaluation and insight into the mesoscale versus synoptic atmospheric dynamics', *Climate Dynamics* **54**(3), 1779–1799.

Van der Hoven, I. (1957), 'Power spectrum of horizontal wind speed in the frequency range from 0.0007 to 900 cycles per hour', *Journal of Atmospheric Sciences* **14**(2), 160–164.

475   Verhoef, A., Portabella, M. and Stoffelen, A. (2012), 'High-resolution ascat scatterometer winds near the coast', *IEEE Transactions on Geoscience and Remote Sensing* **50**(7), 2481–2487.

Vincent, C. L. and Hahmann, A. N. (2015), 'The impact of grid and spectral nudging on the variance of the near-surface wind speed', *Journal of Applied Meteorology and Climatology* **54**(5), 1021–1038.

Vincent, C. L., Pinson, P. and Giebela, G. (2011), 'Wind fluctuations over the north sea', *International Journal of Climatology* **31**(11), 1584–1595.

Vogelzang, J. and Stoffelen, A. (2021), 'Quadruple collocation analysis of in-situ, scatterometer, and NWP winds', **126**(5).

URL: *https://agupubs.onlinelibrary.wiley.com/doi/abs/10.1029/2021JC017189*

Vogelzang, J. and Stoffelen, A. (2022), 'Ascat land correction, v1.0', https://scatterometer.knmi.nl/publications/pdf/ASCAT_land_correction_v1.0.pdf. Accessed: 2023-03-11.

Welch, P. (1967), 'The use of fast fourier transform for the estimation of power spectra: a method based on time averaging over short, modified periodograms', *IEEE Transactions on audio and electroacoustics* **15**(2), 70–73.

Weusthoff, T. and Hauf, T. (2008), 'The life cycle of convective-shower cells under post-frontal conditions', *Quarterly Journal of the Royal Meteorological Society: A journal of the atmospheric sciences, applied meteorology and physical oceanography* **134**(633), 841–857.

Wiese, A., Stanev, E., Koch, W., Behrens, A., Geyer, B. and Staneva, J. (2019), 'The impact of the two-way coupling between wind wave and atmospheric models on the lower atmosphere over the north sea', *Atmosphere* **10**(7), 386.